Derivation of wind fields in dust storm region of clear-sky from FY-2E infrared window imagery using the time difference technique

YANG Lu[1,2], WANG Zhenhui[1,2], ZHAN Yizhe[1,2], ZHANG Zhiguo[1,2]

1. *Key Laboratory of Meteorological Disaster of Ministry of Education, Nanjing University of Information Science & Technology, Nanjing* 210044, *China*;
2. *School of Atmospheric Physics, Nanjing University of Information Science & Technology, Nanjing* 210044, *China*

Abstract: We compute the total increase of the brightness temperature (*T*) from each of the five layers in an FY-2E IR1 w indow imagery which corresponds to 50% and 30% increments in the aerosol extinction coefficient within a half hour p eriod. We used the MODTRAN radiative transfer model under the U. S. standard atmosphere, and analyzed the contributions to the total increment in aerosol extinction coefficient in spring, and the level at which the layered increment in *T* caused by an increment in the aerosol extinction coefficient is absolutely maximal compared with the *T* values of other l evels. We describe a time difference technique based on atmospheric radiative transfer theory, aim to extract the weak aerosol tracer from the FY-2E infrared (IR) window channel with a sensitivity of 0.2 K for clear sky conditions. Both the simulation and case studies results show that we can obtain atmospheric motion vectors (AMVs) in the arid and semi-arid dust outbreak region by tracking the movement of a weak aerosol tracer in the FY-2E infrared (IR) window channel using the time difference technique when traditional cloud tracking does not work due to the lack of clouds. The results are in good a greement with the 850 hPa wind field acquired in National Centers for Environmental P rediction (NCEP) reanalysis data.

Key words: radiative transfer, time difference method, AMVs in clear regions, FY-2E, aerosol

CLC number: TP701 **Document code:** A

Citation format: **Yang L, Wang Z H, Zhan Y Z and Zhang Z G. 2013. Derivation of wind fields in dust storm region of clear-sky from FY-2E infrared window imagery using the time difference technique. Journal of Remote Sensing, 17(5): 1223-1234 [DOI: 10.11834/jrs.20132262]**

1 INTRODUCTION

Wind-related information is one of the most important sets of meteorological data. However, it is not measurable in areas that lack conventional meteorological observation stations. Even in inland regions, the distribution density of conventional stations often makes it difficult to meet the demands of monitoring, analyzing, and forecasting on small and medium scales (such as a gust of wind or shower of rain).

The wind vectors derived from satellites depend mainly on the tracking of clouds in the Visible Satellite Imagery (VIS) and Infrared Satellite Imagery (IR) or by tracking water vapor from the Water Vapor Channel (WVC), and the products are respectively referred to as Cloud Motion Wind (CMW) and water vapor wind (Stewart, et al., 1985; Schmetz, et al., 1993; Velden, et al., 1997). However, clear skies would prevent the occurrence of determining these kinds of vectors using the cloud tracking technique. Water Vapor Channel (WVC) imagery has been used to derive winds, which compensate for this to a certain extent, but if we are also able to use tracers in addition to clouds from IR channel imagery, additional Atmospheric Motion Vectors (AMVs) may be available, especially during clear sky periods.

Atmospheric aerosol refers to all kinds of solid and liquid particles suspended in the atmosphere. Although aerosols account for only one billionth of the total air quality, they have a significant effect on the atmospheric radiation transfer and water cycle (Luo, et al., 2001). Aerosols act as a key factor in the research of climate and environmental changes, significantly impacting the radiation budget in geo-gas systems. The longwave radiation effect of most aerosols is far smaller than the shortwave radiation effect (Shi, 2007). Moreover, dust aerosols with larger particles not only increase the reflection of solar shortwave radiation, but also decrease the downward transmission trends. At the same time, they absorb the longwave radiation on the surface

Received: 2012-09-06; **Accepted:** 2013-04-16; **Version of record first published:** 2013-04-23

Foundation: National Natural Science Foundation of China (No. 41175035, 41005005); National Basic Research Program (No. 2009CB421502); Jiangsu university advantage disciplines construction project funding projects (PAPD)

First author biography: YANG Lu (1988—), female, master candidate, she majors in remote sensing and AMVs technique. E-mail: yanglu_19@sina.com

Corresponding author biography: WANG Zhenhui (1955—), male, professor, his research interest is atmospheric remote sensing and application, and he has published over 50 papers. E-mail: eiap@nuist.edu.cn

and a tmospheric downward reflection of radiation, leading to an increase in temperature above the dust layer and cooling below it.

Zhang, et al. (2002) analyzed the distribution and characteristics of aerosols in China using a sun photometer, ground observation, and satellite remote sensing, and found that the aerosol optical depths correspond to the peak values obtained in the Yellow River, Yangtze river, coastal area, and Sichuan basin all year round. In most areas, the aerosol optical depth is the largest during spring, especially in arid and semi-arid regions where dust particles are common, and the Aerosol Optical Depth (AOD) is significantly greater than in the other seasons. Zhan, et al. (2012) combined the split window and AMWs techniques to retrieve the wind vectors from the 11 μm and 12 μm channels on the VISSR onboard the FY-2E geostationary satellite. The sand aerosol sensitivity analysis for geostationary meteorology satellite IRSW channels has been performed using the MODTRAN radiative transfer model. Using the image difference mask method and treating the dust aerosol as a tracer, effective wind information can be obtained from the arid and semi-arid dust outbreak region in which the conventional AMVs cannot be r etrieved.

The total increase in the brightness temperature in FY-2E IR1 window imagery corresponding to 50% and 30% increments in aerosol extinction coefficient within 0.5 h from each of the five layers has been computed with the MODTRAN radiative transfer model under the U. S. standard atmosphere, and we analyzed the contributions to the total increment in the aerosol extinction coefficient in spring and the level at which the layered increment in T caused by an increment in aerosol extinction coefficient is maximum compared with the T values of other levels. We describe a time difference technique based on atmospheric radiative transfer theory for the extraction of the weak aerosol tracer from the FY-2E infrared (IR) window channel with a sensitivity of 0.2 K for clear sky periods.

2 TIME DIFFERENCE METHOD

The LW radiation measured by the satellite at infrared wavelengths is modified during its passage through the atmosphere. The atmosphere is characterized by the presence of several entities that absorb and emit radiation, such as H_2O and CO_2 molecules, atmospheric aerosol particles, and atmospheric pollutants. Hence, the spectral radiation I_λ observed by the satellite can be expressed as

$$I_\lambda = \varepsilon_\lambda B_\lambda(T_s)\tau_\lambda(0) + \int_0^\infty \alpha_\lambda(z) J_\lambda(z) \tau_\lambda(z)\,\mathrm{d}z \quad (1)$$

where λ represents the wavelength, ε_λ represents the surface emissivity, $B_\lambda(T_s)$ is the Planck function that corresponds to the surface temperature T_s, $B_\lambda(z)$ is the Planck function at height z, α_λ is the atmospheric extinction coefficient (including atmospheric absorption and scattering), $J_\lambda(z)$ is the source function at height z (including the Planck radiation and scattering radiation),

$$\tau_\lambda(z) = \exp\left(-\int_z^\infty \alpha_\lambda(z)\,\mathrm{d}z\right) \quad (2)$$

where $\tau_\lambda(z)$ is the atmospheric transmittance from height z to the top of the atmosphere,

$$\tau_\lambda(0) = \exp\left\{-\int_0^\infty \alpha_\lambda(z)\,\mathrm{d}z\right\} \quad (3)$$

is the atmospheric transmittance for the entire layer. Based on the above analysis, I_λ can also be expressed as

$$I_\lambda = I_\lambda(\varepsilon_s, T_s, T, \alpha_{H_2O}, \beta_{ext}, \alpha_{gas}) \quad (4)$$

that is, the spectral radiation I_λ observed by the satellite in a clear sky is determined by the surface emissivity, surface temperature, atmospheric temperature at one level, water vapor, aerosol e xtinction coefficient, and other ingredients.

Assume that the increment of the spectral radiance in a pixel under observation for a short period $\Delta t(t_2 - t_1)$ is

$$\Delta I_\lambda = I_\lambda^{t_2} - I_\lambda^{t_1} \quad (5)$$

Suppose that Δt is sufficiently short, then

$$\Delta I_\lambda = \frac{\mathrm{d}I_\lambda}{\mathrm{d}t} \cdot \Delta t \quad (6)$$

based on Eq. (4), the total derivative of I_λ respective to t is

$$\frac{\mathrm{d}I_\lambda}{\mathrm{d}t} = \frac{\partial I_\lambda}{\partial \varepsilon_s}\frac{\mathrm{d}\varepsilon_s}{\mathrm{d}t} + \frac{\partial I_\lambda}{\partial T_s}\frac{\mathrm{d}T_s}{\mathrm{d}t} + \frac{\partial I_\lambda}{\partial T(z)}\frac{\mathrm{d}T(z)}{\mathrm{d}t} + \frac{\partial I_\lambda}{\partial \alpha_{H_2O}(z)}\frac{\mathrm{d}\alpha_{H_2O}(z)}{\mathrm{d}t} + \frac{\partial I_\lambda}{\partial \beta_{ext}(z)}\frac{\mathrm{d}\beta_{ext}(z)}{\mathrm{d}t} + \frac{\partial I_\lambda}{\partial \alpha_{gas}(z)}\frac{\mathrm{d}\alpha_{gas}(z)}{\mathrm{d}t} \quad (7)$$

Additionally, in the short Δt period, suppose that the surface emissivity and the other ingredients can be omitted; the surface temperature and atmospheric temperature can be omitted on sea, while on the land, we used the split window difference technique to mitigate the impact of local temperature, then the only term that remains from Eq. (7) for the arid and semi-arid regions (in which there is little water vapor) is expressed as

$$\frac{\mathrm{d}I_\lambda}{\mathrm{d}t} \approx \frac{\partial I_\lambda}{\partial \beta_{ext}(z)}\frac{\mathrm{d}\beta_{ext}(z)}{\mathrm{d}t} \quad (8)$$

based on Eq. (6), we can obtain the numerical expression for Eq. (9) or Eq. (10).

$$\frac{\Delta I_\lambda}{\Delta t} \approx \frac{\partial I_\lambda}{\partial \beta_{ext}(z)}\frac{\Delta \beta_{ext}(z)}{\Delta t} \quad (9)$$

or

$$\Delta I_\lambda \approx \frac{\partial I_\lambda}{\partial \beta_{ext}(z)}\Delta \beta_{ext}(z) \quad (10)$$

Eq. (10) represents the increment of spectral radiation I_λ caused by $\Delta\rho(\mathrm{g/m^3})$. According to Eq. (1), the total increment of I_λ observed by the satellite corresponds to the accumulated value in the entire atmosphere layer.

In the MODTRAN radiative transfer model, we can obtain the equivalent spectral radiance of the FY-2E IR channel by the convolution of the sub-spectral radiance $L_{target}(\lambda)$ observed by the remote sensor and SRF $f_{res}(\lambda)$ of the FY-2E IR channel. Therefore, I_λ in the above formulas can also be written as

$$I_\lambda = \frac{\int L_{target}(\lambda) \cdot f_{res}(\lambda)\,\mathrm{d}\lambda}{\int f_{res}(\lambda)\,\mathrm{d}\lambda} \quad (11)$$

According to the Planck function, we can convert the spectral radiance I_λ into an equivalent brightness temperature

$$I_\lambda = \frac{C_1 \lambda^{-5}}{\exp\left(\frac{C_2}{\lambda T_B}\right) - 1} \quad (12)$$

from this, we can get

$$T = \frac{C_2}{\lambda \ln\left[\frac{C_1}{\lambda^5 I(\lambda)} + 1\right]} \quad (13)$$

where $C_1 = 1.191 \times 10^{-12}$ (W/cm^2/sr/(cm^{-1})^4) is the first radiation constant for the spectral radiance and $C_2 = 1.439$ (K · cm^{-1}) is the second radiation constant for the spectral radiance; T is the brightness temperature (K).

We can obtain the exact numerical derivative of the spectral radiance by using MODTRAN. $\Delta\beta_{ext}$ represents the increment of the aerosol extinction coefficient for a specific narrow height in Δt. By applying Eq. (10) and Eq. (13), we can obtain the exact numerical derivative of the brightness temperature in the FY-2E IR window imagery with respect to the increment of the aerosol extinction coefficient. In this paper, we analyzed the contributions of the total increment of the aerosol extinction c oefficient to the total brightness temperature in spring, and to the height assigned to the derived AMWs in clear sky conditions.

Due to the impact of wind, precipitation, and temperature in spring, there are frequent dust storms in the northern area, and dust aerosol particles will exhibit obvious movement during gale conditions and the diurnal variation of the atmospheric stability (Shen, et al., 2007), which causes the atmospheric aerosol optical depth to exhibit obvious and intense changes in a short period of time. The optical depth may rapidly increase to a very large value, and can increase by 1 or 2 when the dust storm occurs for 0.5—1 h; when the storm ends, the optical depth can quickly r eturn to the basic normal level (Zhang, et al., 2002; Shen, et al., 2007). Therefore, the optical depth can exhibit significant variations in a short period of time in spring during dust storms. In this paper, we set the increment of the aerosol extinction coefficient as 50% in a half-hour period.

Assume that $\frac{\partial I_\lambda}{\partial \rho(z)}$ is constant for a horizontal scale of 80 × 80 km^2, which is taken as the size of a tracer module and $\Delta\beta_{ext}$ represents the advection movement of the aerosol. We can infer that the texture in the subtraction imageries of pairs of three c onsecutive half-hour IR window imageries is caused by the a dvection movement of the aerosol. Therefore, we can obtain the wind fields for clear sky conditions by extracting and tracking the texture motion information, and the height assigned to the derived AMVs in clear sky conditions is basically the level at which there is a maximal increment in *TB* caused by the increment of the aerosol extinction coefficient compared to all other levels.

In this study, the technique described above to derive AMVs in clear sky conditions is referred to as the "time difference method."

3 MODEL CALCULATIONS FOR TIME DIFFERENCE TECHNIQUE

Because the distribution of the aerosol in the space is not u niform, we assumed that the concentration of the aerosol decreases exponentially with an increase in height by referring to Shen (2007), as shown in Eq. (14):

$$N_a(h) \approx N_a(0)\, e^{-h/H_a} \quad (14)$$

where $N_a(0)$ represents the aerosol concentration on the ground, $N_a(h)$ is the aerosol concentration at height h, and H_a refers to the aerosol scale height, which indicates the descent rate of the aerosol as the height increases. In the Peterson Model and K oschmieder Model, the aerosol scale height varies according to the season (Nann & Riordan, 1991). Specifically, the scale height is 1.25 km in spring. From Eq. (14), we obtain

$$\beta_{ext}(h) \approx \beta_{ext}(0)\, e^{-h/H_a} \quad (15)$$

where $\beta_{ext}(0)$ is the aerosol extinction coefficient on the ground and $\beta_{ext}(h)$ refers to the aerosol extinction coefficient at height h. The relationship between the aerosol optical depth and aerosol extinction coefficient can be given as Eq. (16) (Elterman, 1970; Wang, 2004)

$$u_a = \int_0^\infty \beta_{ext}(0)\, e^{-h/H_a}\, dh \approx \beta_{ext}(0)\, H_a \quad (16)$$

Then, the aerosol optical depth at a certain layer is

$$u_h = \int_{h_1}^{h} \beta_{ext}(0)\, e^{-h/H_a}\, dh \quad (17)$$

MODTRAN can obtain the aerosol optical depth from the aerosol extinction coefficient, which is based on V (horizontal meteorological range), season and water vapor amounts. He (2003) provided the empirical relationships between V and the aerosol optical depth corresponding to different seasons according to MODTRAN simulation results Eq. (18).

$$V = \frac{1}{u_h a} - \frac{b}{a} \quad (18)$$

where a and b vary according to the season, aerosol type, and water vapor content. According to his study, we selected values of $a = 0.1202$ and $b = 0.2974$ in spring.

To simulate the aerosol profile, we assume that the aerosol optical depth of the whole atmosphere is 1.0 (Guan & Li, 2010) and the aerosol scale height is 1.25 km. According to Eq. (16), the aerosol extinction coefficient on the ground $\beta_{ext}(0)$ is 0.80. U sing $\beta_{ext}(0)$ in Eq. (17), the aerosol optical depth of each layer can be calculated, and will determine the horizontal mete-o rological range, which is required by MODTRAN in E q. (18). The surface temperature was set to 292 K and the water vapor content was set to 0.3 g/cm^2. We calculated the increment of the brightness temperature caused by the 50% increase in the aerosol extinction coefficient of each layer from 0 km to 5 km. The r esults are shown in Table 1. The columns from left to right in the table r espectively refer to the height, pressure, temperature, water vapor volume ratio in ppm (weight), aerosol extinction c oefficient, aerosol optical depth, horizontal meteorological range, the derivative of the brightness temperature respective to aerosol extinction coefficient in IR1 channel, and the increment in the brightness temperature for each layer. It can be seen from Table 1 that the total increment in T reaches −0.379 K, which is the sum of the last column in Table 1, and is almost twice as much as the temperature-sensitivity threshold (0.2 K) of the F Y-2E IR window channel (assuming that the aerosol above 5 km is negligible). The increment in T caused by the increment of the aerosol extinction coefficient is maximal below 2 km. Through further calculation, a 30% increment in the aerosol e xtinction coefficient in a half-hour period can make the increment in T reach −0.210 K, which is more than the temperature-sensitivity threshold of the FY-2E IR window channel. This indicates that the FY-2E satellite can observe this signal through a dust storm.

Table 1 The profile of the aerosol parameter and the increment of the brightness temperature caused by a 50% increase in the aerosol extinction coefficient in the U. S. standard atmosphere in spring

h/km	P/hPa	T/K	H_2O/PPMV	$\beta_{ext}(h)$	AOD	V/km	$\frac{\partial T}{\partial \beta_{ext}(h)}$	ΔT/K
0	1013.3	288.2	1080	0.800	0.55	12.66	-0.340	-0.173
1	898.8	281.7	721	0.359	0.25	30.81	-0.598	-0.107
2	795.0	275.2	691	0.160	0.11	73.16	-0.713	-0.057
3	701.2	268.7	224	0.072	0.05	163.92	-0.750	-0.032
4	616.6	262.2	137	0.032	0.03	274.85	-0.563	-0.009
5	540.5	255.7	80	0.0015	0.002	4157.26	-1.333	-0.001

4 CASE STUDIES

4.1 Analysis of weather process

To determine the impact of strong cold air and Mongolia cyclones, we observed the case for a dust storm that engulfed the Nanjiang basin, the east part of northwest China, central and western regions of Inner Mongolia, north China, and west part of northeast China from April 28 to 30, 2011. Of these areas, the Nanjiang basin, west part of Gansu province, and west part of Inner Mongolia suffered particularly from the strong dust storm. This dust weather was the strongest and most extensive in area since the spring of the previous year.

4.2 Case studies in clear-sky conditions

We chose three sets of longitude-latitude-projected IR images observed by FY-2E during the period 05:01—06:01 (UTC) on April 28 and 06:01—07:01 on April 30, 2011. Then, they were used to conduct cloud masking, time difference p rocessing, and linear increase, and then applied to the Cloud-Motion Wind Inferring System (CWIS), which was developed by Wang and Zeng(1996). By tracking the movement of aerosol s ignals from FY-2E IR window imagery, we obtained the AMVs retrieved from the method mentioned above. The results are shown in Fig. 1 and Fig. 2. Because cloud imaging cannot c ompletely cover the cloud area, we compared it with the cloud motion winds (Fig. 1(b)) from the National Satellite Mete-o rological Center (NSMC), and took the area outlined by rectangle A as the experimental area.

Fig. 1(a) shows the CMWs retrieved from the original IR imagery with CWIS at 05:01 on April 28. Fig. 1(c) gives the 850 hPa wind field of the NCEP reanalysis data for comparison. It can be seen that in the central and northern parts of Mongolia (rectangle A), which refers to the clear sky area, we can obtain the wind field using the time difference method by tracking the aerosol signals in Fig. 1(c), and the method has basically c overed the clear sky area, whereas the conventional CMW technique fails in this regard.

It would be better to validate the AMVs retrieved from the time difference technique presented above by using the real o bservational data in that area. By following the studies involving the validation of NCEP reanalysis data done by Zhu, et al. (2012) and Su, et al. (1999), we compared it with the 850 hPa wind field of NCEP reanalysis data. It can be seen that the wind directions are almost consistent with each other, both represent west or southwest directions and the average wind speed obtained using the time difference technique is 8 m/s, which is relatively higher than the wind speed in Fig. 1(d).

On the morning of April 30, a sandstorm appeared in the central and eastern regions of Inner Mongolia, north of Shanxi province, Hebei province, and the western part of northeast China. The CMW results obtained from the original IR imagery with CWIS and from the National Weather Meteorological Center at 06:01 of April 30, 2011 are shown in Fig. 2(a) and Fig. 2(b), respectively. Fig. 2(c) shows the AMWs retrieved using the time difference technique. Fig. 2(d) shows the 850 hPa wind field of NCEP reanalysis data at 06:00 on April 30, 2011. It can be seen from Fig. 2(a) and Fig. 2(b) that there are no wind vectors in the central and eastern regions of Inner Mongolia and the north of Shanxi province. In Fig. 2(a), the regions that refer to the clear-sky area appear dark. In this case, we can obtain the wind field from the time difference method by tracking the aerosol signals in Fig. 2(c), and the method has basically covered the clear sky area that is not covered by the conventional CMW technique.

Compared with the 850 hPa wind field of NCEP reanalysis data (Fig. 2(d)), we can see that the wind direction retrieved from the time difference technique for the clear-sky region is northwest, which is consistent with the directions observed in the NCEP r eanalysis data. In the middle of Inner Mongolia, the average wind speed obtained using the time difference technique for clear-sky conditions is 8 m/s, which is 4—6 m/s smaller than those values obtained in NCEP reanalysis data. In the northern part of Shanxi, the average wind speed retrieved using the time difference technique is consistent with that in the NCEP reanalysis data.

5 CONCLUSION

The total increment in brightness temperature in FY-2E IR1 window imagery corresponding to a 50% and 30% increment in the aerosol extinction coefficient within a half-hour period from each of the 5 layers was computed with the MODTRAN radiative transfer model under the U. S. standard atmosphere. Also, we analyzed the contributions to the total increment in the aerosol extinction coefficient in spring and the layer at which the increment in T caused by an increment in the aerosol extinction coefficient is the most among all five layers. From the simulation result, the total increment in T reaches -0.379 K, and is maximal below 2 km. Also, a 30% increment in the aerosol extinction c oefficient within a 0.5 h period can make the increment in T reach -0.

210 K, which is more than the temperature-sensitivity threshold of the FY-2E IR window channel. This indicates that FY-2E IR1 window imagery can be used to derive wind fields for clear-sky regions under certain conditions.

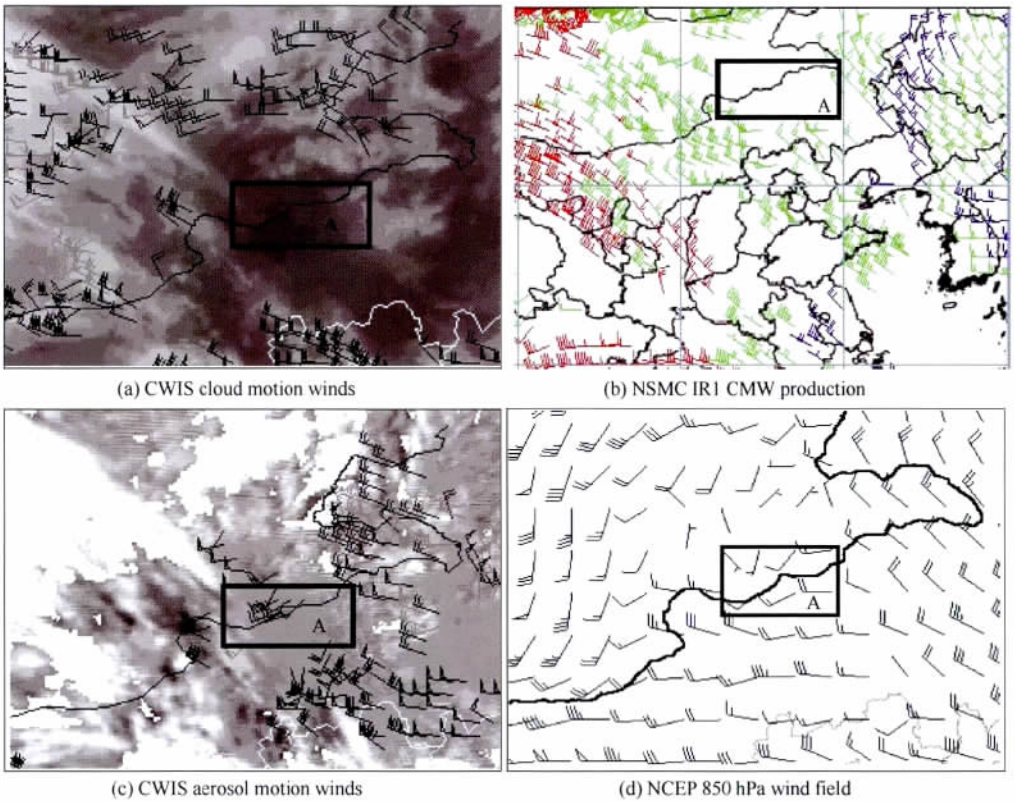

(a) CWIS cloud motion winds (b) NSMC IR1 CMW production

(c) CWIS aerosol motion winds (d) NCEP 850 hPa wind field

Fig.1 AMVs comparison analysis for the case in area A on April 28, 2011

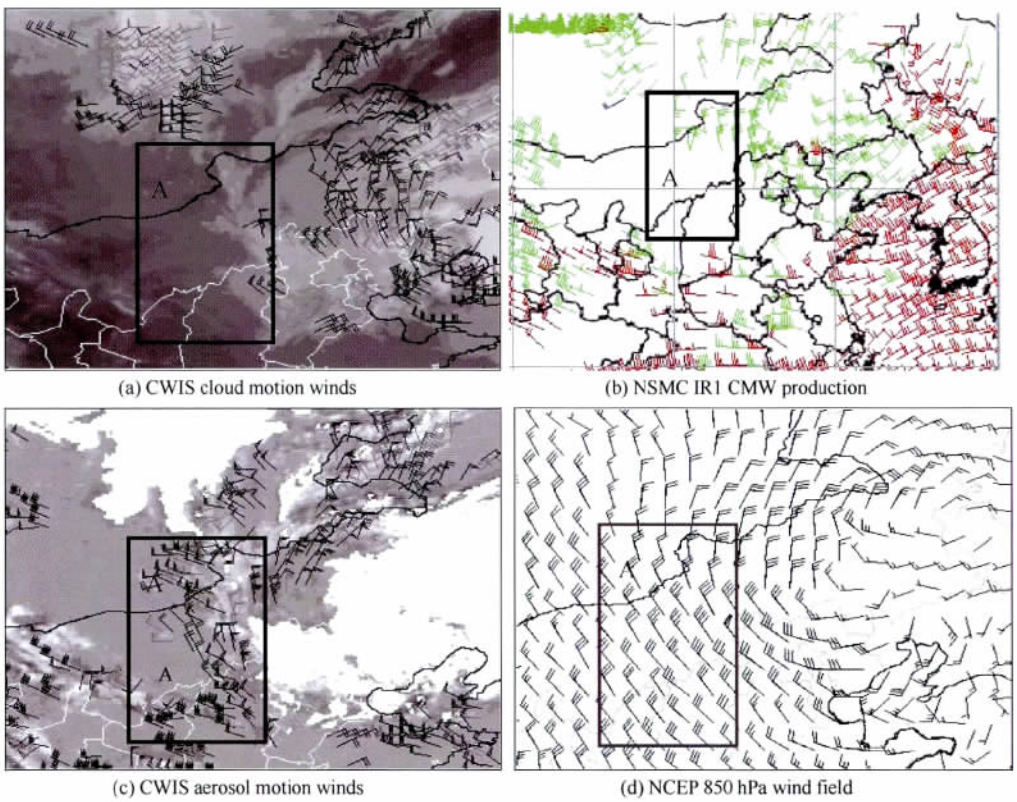

(a) CWIS cloud motion winds (b) NSMC IR1 CMW production

(c) CWIS aerosol motion winds (d) NCEP 850 hPa wind field

Fig.2 AMVs comparison analysis for the case in area A on April 30, 2011

Case studies were presented to verify the simulation analysis, and the results show that by tracking the movement of aerosol in clear sky conditions using the time difference technique, AMVs, rather than traditional CMW, have been o btained. The obtained AMVs are in good agreement with the 850 hPa wind field of the NCEP reanalysis data, which provide useful information and supplement the monitoring of the sandstorm's motion.

It should be noted that the extraction of sand aerosol motion signals mainly depend on the increase in the brightness temperature that resulted from by the increase of sand aerosol. Furthermore, we can trace additional texture features caused by more obvious motion of the sand aerosol, which will improve the a pplicability and accuracy of this method. Otherwise, we cannot use sand aerosol as a tracer. Moreover, this paper focuses mainly on the theoretical derivation, and did not study the feasibility of different atmospheric conditions, regions, and seasons. Also, the height assigned to the aerosol motion winds is mainly in the boundary layer, which needs to be verified in a future study.

REFERENCES

Berk A, Anderson G P, Acharya P K, Hoke M L, Chetwynd J H, Bernstein L S, Shettle E P, Matthew M W and Adler-Golden S M. 2003. MODTRAN 4 Version 3 Revision 1 User's Manual, Manual, Air Force Research Laboratory. Hanscom Air Force Base, MA: Air Force Res Lab

Elterman L. 1970. Vertical-Attenuation model with Eight surface Meteorological Ranges 2 to 13 Kilometers. Environment Research Paper, NO. 318, AFCRL-70-200

Guan J X and Li C C. 2010. Spatial distributions and changes of aerosol optical depth over Eastern and Central China. Acta Scientiarum Naturalium Universitatis Pekinensis, 46(2): 186-191

He L M, Wang H, Yan G J, Li X W, Zhu W J and Wang J D. 2003. Analysis and application for the empirical relative between aerosol optical depth and horizontal meteorological range. Journal of Remote Sensing, 7(5): 372-378

Luo Y F, Li W L and Zhou X J. 2001. Analysis of the 1980's atmospheric aerosol optical depth over China. Acta Meteorologica Sinica, 59(1): 77-87

Nann S and Riordan C. 1991. Solar spectral irradiance under clear and cloudy skies: measurements and a semiempirical model. Journal of Applied Meteorology, 30(4): 447-462 [DOI: 10.1175/1520-0450(1991)030<0447:SSIUCA>2.0.CO;2]

Shi G Y. 2007. Atmospheric Radiology. Beijing: Science Press, 261-264

Shen J G, Li J P, Niu S J and Jiang X G. 2007. Spatial-temporal distribution of aerosol optical properties during Sand-dust weather processes. Journal of Desert Research, 27(3): 495-501

Schmetz J, Holmlund K, Hoffman J, Strauss B, Mason B, Gaertner V, Koch A and Van De Berg L. 1993. Operational cloud-motion winds from Meteosat infrared images. Journal of Applied Meteorology, 32(7): 1206-1225 [DOI: 10.1175/1520-0450(1993)032<1206:OCMWFM>2.0.CO;2]

Stewart T R, Smith W L and Hayden C M. 1985. A note on water-vapor wind tracking using VAS data on McIDAs. Bulletin of the American Meteorological Society, 66(9): 1111-1115 [DOI: 10.1175/1520-0477(1985)066<1111:ANOWVW>2.0.CO;2]

Su Z X, Lv S H and Luo S W. 1999. The examinations and analysis of NCEP/NCAR 40 years global reanalysis data in China. Plateau Meteorology, 18(2): 209-218

Velden C S, Hayden C M, Nieman S J, Menzel W P, Wanzong S and Goerss J S. 1997. Upper-Tropospheric Winds Derived from Geostationary Satellite Water Vapor Observations. Bulletin of the American Meteorological Society, 78(2): 173-195 [DOI: 10.1175/1520-0477(1997)078<0173:UTWDFG>2.0.CO;2]

Wang Y. 2004. The Research of Target Background Contrast and Atmospheric Visibility in the Atmosphere. Hefei: Chinese Academy of Sciences Institute of Optics and Fine Mechanics in Anhui Province

Wang Z H and Zeng W L. 1996. A pc-based objective inferring system for cloud motion winds from geostationary satellite images. Journal of Nanjing Institute of Meteorology, 19(1): 69-75

Zhan Y Z, Wang Z H and Zhang Z G. 2012. Wind fields in dust storm clear sky region from the FY-2E split window channels. Journal of Remote Sensing, 16(4): 738-750

Zhang J H, Mao J T and Wang M H. 2002. Analysis of the aerosol extinction characteristics in different areas of China. Advances in Atmospheric Sciences, 19(1): 136-152 [DOI: 10.1007/s00376-002-0040-x]

Zhu Y L, Ling C, Chen H B, Zhang J Q, Peng L and Yu Y. 2012. Comparison of two reanalysis data with the RS92 radiosonde data. Climatic and Environmental Research, 17(3): 381-391

FY-2E 红外通道晴空沙尘区时间差分法导风研究

杨璐[1,2]，王振会[1,2]，詹奕哲[1,2]，张治国[1,2]

1. 南京信息工程大学 气象灾害省部共建教育部重点实验室，江苏 南京 210044;
2. 南京信息工程大学 大气物理学院，江苏 南京 210044

摘　要: 利用大气红外辐射传输模式，结合 FY-2E 静止卫星红外窗区光谱响应函数，模拟计算了标准大气环境下 0—5 km 各高度层气溶胶消光系数增量为 50% 和 30% 两种情况下对 FY-2E 红外 1 通道亮温增量的贡献。定量分析了春季气溶胶消光系数对亮温增量的影响以及主要影响高度。结合 FY-2E 红外 1 通道灵敏度，提出了可用于红外通道晴空沙尘气溶胶微弱示踪信号移动追踪的“时间差分法”。理论模拟计算和实例分析表明，在一定条件下，“时间差分法”追踪红外通道晴空沙尘气溶胶微弱示踪信号的移动，可以获得传统云导风所无法得到的干旱半干旱沙尘爆发区的风场信息，且反演得到的风场与美国国家环境预报中心 NCEP 再分析资料 850 hPa 风场有着很好的一致性。

关键词: 辐射传输，时间差分法，晴空导风，FY-2E，气溶胶

中图分类号: TP701　　**文献标志码**: A

引用格式: 杨璐，王振会，詹奕哲，张治国. 2013. FY-2E 红外通道晴空沙尘区时间差分法导风研究. 遥感学报，17(5): 1223－1234

Yang L, Wang Z H, Zhan Y Z and Zhang Z G. 2013. Derivation of wind fields in dust storm region of clear-sky from FY-2E infrared window imagery using the time difference technique. Journal of Remote Sensing, 17(5): 1223－1234 [DOI: 10.11834/jrs.20132262]

1　引　言

风向和风速是非常重要的气象资料。但在海洋、沙漠等测站稀少地区，风场观测资料极其缺乏。即使在内陆地区，气象常规观测站的分布密度也常常难以满足中小尺度(如阵风、阵雨等对流性天气)现象的监测、分析和预报的需求。

目前的卫星导风，主要是通过追踪气象卫星可见光和红外云图序列上的云以及水汽图上水汽的位移来计算大气运动矢量(Stewart 等，1985; Schmetz 等，1993; Velden 等，1997)，分别称为云迹风和水汽风。但在不能被识别为“云”的区域(本文称为“晴空区”)，基于云图的云导风技术无法获得风矢。基于水汽图的水汽导风可以在一定程度上弥补“晴空区”缺少的云迹风矢。但是，除云和水汽可作为示踪物外，如果卫星导风还能利用其他信息，则可进一步补充人们渴求的大气运动信息。

大气气溶胶是指大气中悬浮着的各种固体和液体粒子。虽然气溶胶质量仅占整个大气质量的十亿分之一，但其对大气辐射传输和水循环均有重要的影响(罗云峰 等，2001)。气溶胶作为影响地气系统辐射收支的重要因子，对气候和环境变化的影响已经成为研究热点。多数气溶胶的长波辐射效应远小于短波辐射效应(石广玉，2007)。而沙尘气溶胶具有较大粒径，增加了对太阳短波辐射的反射，使向下透射减小; 同时又吸收地表发射长波辐射和大气下行辐射的反射，导致沙尘层以上大气增温而沙尘层以下大气冷却。

Zhang 等人(2002)利用太阳光度计、地面观测和卫星遥感等对中国地区气溶胶的分布和特性进行研究，发现黄河、长江中下游及沿海地区、四川盆地附近，全年都是气溶胶光学厚度的极大值中心; 全国

收稿日期: 2012-09-06; 修订日期: 2013-04-16; 优先数字出版日期: 2013-04-23

基金项目: 国家自然科学基金(编号: 41175035，41005005); 国家重点基础研究发展计划(973 计划)(编号: 2009CB421502); 江苏高校优势学科建设工程资助项目(PAPD)

第一作者简介: 杨璐(1988—)，女，硕士，主要从事卫星资料应用研究。E-mail: yanglu_19@sina.com

通信作者简介: 王振会(1955—)，男，教授，博士生导师，现从事大气遥感应用研究。已发表论文 50 余篇。E-mail: eiap@nuist.edu.cn

大部分地区在春季气溶胶光学厚度最大,尤其在干旱半干旱地区,春季气溶胶光学厚度明显大于其他季节,且大多为沙尘粒子。詹奕哲等人(2012)将红外分裂窗差值监测沙尘的技术及卫星导风技术相结合,针对 FY-2E 气象卫星,利用 MODTRAN 辐射传输模式对沙尘晴空区特征进行敏感性分析,再将经过图像掩模及线性处理后的分裂窗差值图像代入导风计算程序计算,获得了传统卫星导风所无法得到的水汽含量低值区风场信息。

本文利用大气辐射传输模式,结合 FY-2E 静止卫星光谱响应函数,在标准大气条件下进行气溶胶增量对亮温增量的模拟计算,定量分析春季大气条件下(气溶胶消光系数半小时内变化 50% 和 30% 两种情况),气溶胶变分对卫星红外 1 通道观测亮温变分的影响大小以及主要影响高度,结合 FY-2E 红外 1 通道灵敏度,提出了使用时间差分技术从静止卫星红外云图提取气溶胶微弱示踪信号的理论和方法。

2 时间差分法理论

红外窗波段是气象卫星进行红外探测的重要通道。虽然这个波段十分透明,卫星遥感可以提供地表和海面的信息,但在实际大气中,辐射传输仍然受到大气中 H_2O、CO_2 等各种气体、大气气溶胶粒子和大气污染物的影响。因此,卫星红外窗通道观测地球大气得到的辐射量 I_λ 可表示为

$$I_\lambda = \varepsilon_\lambda B_\lambda(T_s)\tau_\lambda(0) + \int_0^\infty \alpha_\lambda(z) J_\lambda(z) \tau_\lambda(z)\,\mathrm{d}z \tag{1}$$

式中,λ 为波长,ε_λ 为地表发射率,$B_\lambda(T_s)$ 为地表温度 T_s 时的普朗克辐射,α_λ 为大气消光系数(含大气吸收与散射衰减),$J_\lambda(z)$ 为高度 z 处大气薄层的源函数(含普朗克辐射和散射辐射),$\tau_\lambda(z)$ 为从高度 z 到大气顶的大气透过率,如式(2)所示

$$\tau_\lambda(z) = \exp\left(-\int_z^\infty \alpha_\lambda(z)\,\mathrm{d}z\right) \tag{2}$$

$\tau_\lambda(0)$ 为整层大气透过率

$$\tau_\lambda(0) = \exp\left\{-\int_0^\infty \alpha_\lambda(z)\,\mathrm{d}z\right\} \tag{3}$$

根据以上分析,I_λ 也可以表示为

$$I_\lambda = I_\lambda(\varepsilon_s, T_s, T, \alpha_{H_2O}, \beta_{ext}, \alpha_{gas}) \tag{4}$$

即卫星观测到的晴空区辐射量 I_λ 受地表比辐射率、地表温度、某一高度层的大气温度、水汽吸收系数、气溶胶消光系数和其余气体吸收系数 6 个因素影响。

假设红外通道图像上晴空区某像元辐亮度 I_λ 在 $\Delta t(t_2 - t_1)$ 时段内的变化为

$$\Delta I_\lambda = I_\lambda^{t_2} - I_\lambda^{t_1} \tag{5}$$

如果 Δt 足够小,则

$$\Delta I_\lambda = \frac{\mathrm{d}I_\lambda}{\mathrm{d}t} \cdot \Delta t \tag{6}$$

对式(4)求全导数可得

$$\frac{\mathrm{d}I_\lambda}{\mathrm{d}t} = \frac{\partial I_\lambda}{\partial \varepsilon_s}\frac{\mathrm{d}\varepsilon_s}{\mathrm{d}t} + \frac{\partial I_\lambda}{\partial T_s}\frac{\mathrm{d}T_s}{\mathrm{d}t} + \frac{\partial I_\lambda}{\partial T(z)}\frac{\mathrm{d}T(z)}{\mathrm{d}t} + \frac{\partial I_\lambda}{\partial \alpha_{H_2O}(z)}\frac{\mathrm{d}\alpha_{H_2O}(z)}{\mathrm{d}t} + \frac{\partial I_\lambda}{\partial \beta_{ext}(z)}\frac{\mathrm{d}\beta_{ext}(z)}{\mathrm{d}t} + \frac{\partial I_\lambda}{\partial \alpha_{gas}(z)}\frac{\mathrm{d}\alpha_{gas}(z)}{\mathrm{d}t} \tag{7}$$

进一步假设在 Δt 时段内地表比辐射率及其余气体含量变化可以忽略;地表温度、大气温度,在海洋上 Δt 时段内可以近似认为不变,故在进行海洋上晴空导风的研究中,可忽略不计;而在研究陆面上的晴空导风时,局地地表温度变化项在 Δt 时段内变化较大,本文利用分裂窗差分的手段减去局地温度变化项的干扰,则对于水汽含量极低的干旱半干旱地区,上式右侧仅剩 1 项,为

$$\frac{\mathrm{d}I_\lambda}{\mathrm{d}t} \approx \frac{\partial I_\lambda}{\partial \beta_{ext}(z)}\frac{\mathrm{d}\beta_{ext}(z)}{\mathrm{d}t} \tag{8}$$

由式(6)可得

$$\frac{\Delta I_\lambda}{\Delta t} \approx \frac{\partial I_\lambda}{\partial \beta_{ext}(z)}\frac{\Delta\beta_{ext}(z)}{\Delta t} \tag{9}$$

或者

$$\Delta I_\lambda \approx \frac{\partial I_\lambda}{\partial \beta_{ext}(z)}\Delta\beta_{ext}(z) \tag{10}$$

由于式(10)右边代表在高度 z 处的大气薄层内气溶胶的增量对辐射量 I_λ 增量的贡献。卫星观测的辐射量如式(1)所示,所以其增量应该是所有大气薄层上的增量的总和。

MODTRAN 是基于辐射传输方程式(1)的辐射传输模式。在该模式中,利用遥感器入瞳处的分谱辐亮度 $L_{target}(\lambda)$ 与 FY-2E 传感器热红外通道光谱响应函数 $f_{res}(\lambda)$ 进行卷积,可以得到 FY-2E 卫星红外窗区某一通道入瞳处的通道等效辐亮度:

$$I_\lambda = \frac{\int L_{target}(\lambda) \cdot f_{res}(\lambda)\,\mathrm{d}\lambda}{\int f_{res}(\lambda)\,\mathrm{d}\lambda} \tag{11}$$

再利用普朗克函数:

$$I_\lambda = \frac{C_1\lambda^{-5}}{\exp\left(\frac{C_2}{\lambda T}\right)-1} \tag{12}$$

可以得到对应通道的亮温:

$$T = \frac{C_2}{\lambda\ln\left[\frac{C_1}{\lambda^5 I(\lambda)}+1\right]} \tag{13}$$

式中,C_1 是第 1 辐射常数,$C_1 = 2hc^2$,等于 1.191×10^{-12},单位为 $W/cm^2/sr/(cm^{-1})^4$,h 为普朗克常数,c 为光速; C_2 为第 2 辐射常数,$C_2 = hc/k$,等于 1.439 K·cm^{-1},其中 k 为波尔兹曼常数。T 为温度,单位为 K。

利用 MODTRAN 可以计算出 $\frac{\partial I_\lambda}{\partial\beta_{ext}(z)}$ 在各高度层的大小。式(10)中 $\Delta\beta_{ext}$ 为 Δt 时段内大气某薄层气溶胶消光系数的变化量。给出一定大气状态下式(10)右边各项的大小,并结合式(13)计算出 $\frac{\partial T}{\partial\beta_{ext}(h)}$ 在各高度层的大小,就可得到气溶胶消光系数的增量对亮温增量的贡献。下面分析春季大气条件下,气溶胶增量对红外 1 通道卫星观测亮温增量的影响大小以及主要影响高度。

春季由于受到风速、风向、降水和气温等气候因素影响,北方地区起沙活动明显,在沙尘天气过程中,沙尘气溶胶粒子在大风的作用下会出现大范围的移动,再加上大气稳定度的日变化(沈建国 等,2007),使得大气气溶胶光学厚度在短时间内变化非常明显,也很剧烈,从没有沙尘天气到发生沙尘天气,光学厚度值可能迅速增大,在 0.5—1 h 之内光学厚度可以从小于 1 增大到 2 以上,而在沙尘天气后期到结束,光学厚度又能很快地恢复到正常的水平(Zhang 等,2002; 沈建国 等,2007)。所以春季发生沙尘天气时,光学厚度变化量在短时间内会很大。在后面的模拟计算中将取 0.5 h 内气溶胶消光系数变化 50%(这等同于光学厚度变化 50%)。

假设在 0.5 h 内,卫星导风示踪模块常用的水平尺度范围内(一般取 80×80 km^2),$\frac{\partial I_\lambda}{\partial\beta_{ext}(z)}$ 是常数,则差值图 ΔI_λ 的纹理就代表 $\Delta\beta_{ext}$ 的纹理。另外,认为 $\Delta\beta_{ext}$ 主要是由于大气气溶胶的平流运动产生,则卫星红外通道两相邻时刻图像的差值图纹理的运动就代表 $\Delta\beta_{ext}$ 的纹理运动,可以通过追踪计算该纹理运动信息来反演相应高度层上大气的运动,其代表高度是影响卫星辐射观测量增量的主要因素所在高度。

基于以上理论的晴空大气风矢计算方法,称为"时间差分法"。

3 时间差分法模拟计算

大气气溶胶含量的空间分布不均匀,参照沈建国等人(2007),取在近地面气溶胶浓度随着高度增加按指数逐步减少,即:

$$N_a(h) \approx N_a(0)\,e^{-h/H_a} \tag{14}$$

式中,$N_a(0)$ 为地面气溶胶浓度,$N_a(h)$ 为在高度 h 处的气溶胶浓度,H_a 为标高,用来表示气溶胶浓度随高度增加而减少的速率,Peterson 模型和 Koschmieder模型中气溶胶标高 H_a 值(Nann 和 Riordan,1991)的选取随季节变化,春季取为 1.25 km。由式(14)可得:

$$\beta_{ext}(h) \approx \beta_{ext}(0)\,e^{-h/H_a} \tag{15}$$

式中,$\beta_{ext}(0)$ 为地面的气溶胶消光系数,$\beta_{ext}(h)$ 为在高度为 h 处的气溶胶消光系数。由式(15)可得整个大气的气溶胶光学厚度与近地面气溶胶消光系数的关系(Elterman,1970; 王毅,2004):

$$u_a = \int_0^\infty \beta_{ext}(0)\,e^{-h/H_a}dh \approx \beta_{ext}(0)\,H_a \tag{16}$$

则某一层气溶胶光学厚度

$$u_h = \int_{h_1}^{h_2}\beta_{ext}(0)\,e^{-h/H_a}dh \tag{17}$$

MODTRAN 模型要求输入水平气象视距 V,然后根据 V 和用户选择的季节、水汽量等插值得到消光系数,最后,对高度积分得到气溶胶光学厚度(Berk 等,2003)。何立明等人(2003)根据 MODTRAN 的模拟结果归纳出不同季节水平气象视距和气溶胶光学厚度的经验公式

$$V = \frac{1}{u_h a} - \frac{b}{a} \tag{18}$$

式中,a 和 b 两个参数在不同季节、气溶胶类型和水汽含量下取值不同。本文参考何立明等人(2003)的结论,选取城市型气溶胶,在水汽含量很小时,春季取 $a=0.1202$,$b=0.2974$。

为模拟气溶胶垂直廓线,假定整个大气的气溶胶光学厚度为 1.0(关佳欣和李成才,2010);气溶胶标高取为 1.25 km,则根据式(16)可以得到地面气溶胶消光系数 $\beta_{ext}(0)$ 为 0.80。将 $\beta_{ext}(0)$ 代入式(17),可以得到春季各个高度层对应的气溶胶光学厚度,再由式(18)可以换算为 MODTRAN 输入所需要的水平气象视距。设定地表温度为 292 K,水汽

含量为0.3 g/cm^2,计算春季0—5 km各高度层气溶胶消光系数50%的增量时,对亮温增量的贡献,如表1所示。表中各列从左到右依次是大气高度、气压、温度、水汽体积比、气溶胶消光系数、气溶胶光学厚度AOD、气溶胶水平气象视距、红外1通道亮温随气溶胶消光系数的变化率及红外1通道气溶胶消光系数50%的增量对亮温增量ΔT的贡献。可见,0—5 km高度层(假设5 km以上气溶胶影响可以忽略)气溶胶消光系数50%的增量能引起亮温变化-0.379 K(即表中最后一列之和),且在2 km以下气溶胶增量对亮温的变化贡献最大。亮温总增量绝对值几乎为FY-2E星载辐射计红外分裂窗通道温度灵敏度0.2 K的2倍。气溶胶消光系数变化量由50%降低为30%,对应的亮温变化为-0.210 K,也大于FY-2E红外窗通道灵敏度。所以,在沙尘天气条件下,FY-2E红外1通道应该可以观测到此信息。

表1 美国标准大气条件下春季气溶胶参量垂直分布特征以及消光系数50%的增量对亮温增量的贡献

h/km	P/hPa	T/K	H_2O/PPMV	$\beta_{ext}(h)$	AOD	V/km	$\frac{\partial T}{\partial \beta_{ext}(h)}$	ΔT/K
0	1013.3	288.2	1080	0.800	0.55	12.66	-0.340	-0.173
1	898.8	281.7	721	0.359	0.25	30.81	-0.598	-0.107
2	795.0	275.2	691	0.160	0.11	73.16	-0.713	-0.057
3	701.2	268.7	224	0.072	0.05	163.92	-0.750	-0.032
4	616.6	262.2	137	0.032	0.03	274.85	-0.563	-0.009
5	540.5	255.7	80	0.0015	0.002	4157.26	-1.333	-0.001

4 个例分析

4.1 天气过程分析

2011年4月28日至30日,受较强冷空气和蒙古气旋影响,中国南疆盆地、西北地区东部、内蒙古中西部、华北大部和东北地区西部相继出现沙尘天气,其中南疆盆地、甘肃西部和内蒙古西部的局地发生沙尘暴或强沙尘暴。此次沙尘天气是2013年入春以来中国北方地区遭受的强度最大、影响范围最广的一次沙尘天气过程。

4.2 晴空导风试验

采用王振会和曾维麟(1996)开发的静止气象卫星云迹风客观导出系统CWIS,先后选取了以2011年4月28日5:01及4月30日6:01(本文所指时间均为世界时)为参考时间的连续3张0.5 h间隔的FY-2E等经纬投影红外1通道云图,进行云图掩模和时间差分处理后,再将差分后的图像进行线性增强,最后通过追踪红外通道晴空区上微弱示踪信号沙尘气溶胶的移动进行了风场反演。结果分别如图1、图2所示。由于时间差分时云掩模不能把云完全覆盖,为了避免云移动造成的风矢的干扰,选取国家卫星中心提供的红外1通道云导风结果(图1(b))进行对比,选取框图A区作为晴空实验区。

图1(a)为2011年4月28日5:01 CWIS(Cloud Motion Wind Inferring System)红外1通道云导风结果。图1(c)是本研究导出的气溶胶沙尘风场,图1(d)为2011年4月28日6:00 NCEP再分析资料的850 hPa风场。从图中可以看出,在内蒙古中部偏北地区(框区A所示),无论在图1(a)和图1(b)上均呈现黑色,属于传统红外通道云导风所无法得到的晴空区或少云区。使用时间差分法,可以得到如图1(c)所示的时间差分图像,图像上可以较为清楚地看到原来被忽视的沙尘气溶胶纹理,通过追踪差分增强图像上的沙尘气溶胶,得到如图所示的晴空风区风矢量。

为验证图1(c)结果的可靠性,需有该时刻该区域的准确观测资料。受条件限制,根据朱彦良等人(2012)、苏志侠等人(1999)对NCEP再分析资料可靠性的研究,我们与图1(d)的NCEP再分析资料的850 hPa风场进行相应区域对比,可以看出,反演得到的晴空风场呈西风偏西南风向,平均风速为8 m/s;NCEP再分析资料相应区域内风场也是西风偏西南风向,平均风速为6 m/s,二者有较好的一致性。

4月30日清晨开始,内蒙古中东部、山西北部、河北北部和东北地区西部部分地区出现沙尘天气。图2(a)(b)分别为2011年4月30日6:01 CWIS红外1通道云导风结果及5:30国家卫星中心红外1通道云导风结果。图2(c)是本研究导出的气溶胶沙尘风场,图2(d)为2011年4月30日6:00 NCEP再分

析资料的 850 hPa 风场。图中框区 A 为晴空导风实验对比区。从图中可以看出，在内蒙古中东部、山西北部，无论是图 2(a) 还是图 2(b) ，都无法得到风矢，从图 2(a) 可以看出，这片区域呈现黑色，属于传统红

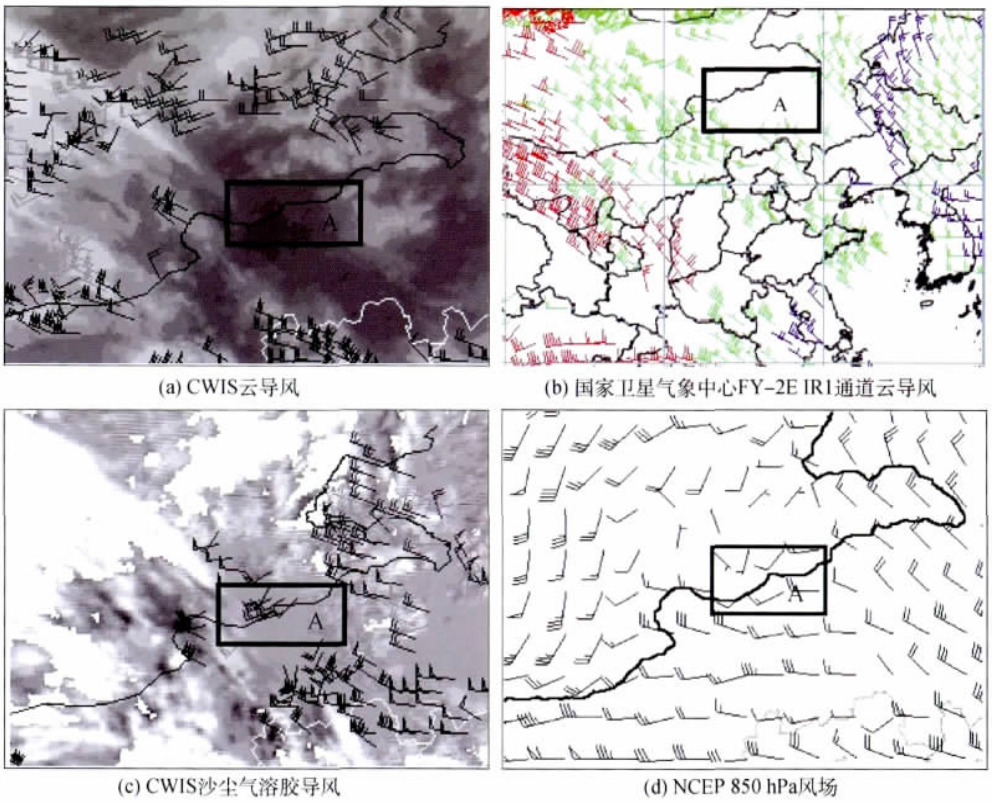

(a) CWIS云导风 (b) 国家卫星气象中心FY-2E IR1通道云导风

(c) CWIS沙尘气溶胶导风 (d) NCEP 850 hPa风场

图 1 2011-04-28 导风个例分析

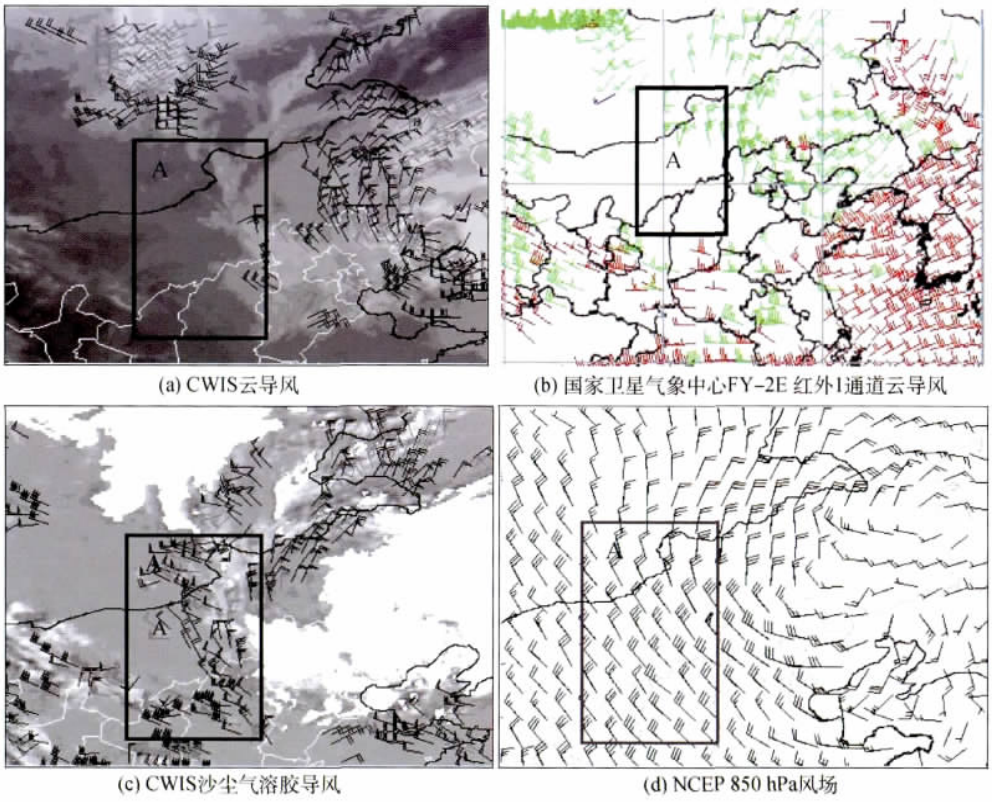

(a) CWIS云导风 (b) 国家卫星气象中心FY-2E 红外1通道云导风

(c) CWIS沙尘气溶胶导风 (d) NCEP 850 hPa风场

图 2 2011-04-30 导风个例分析

外通道云导风所无法得到的晴空区或少云区。使用时间差分法,得到如图 2(c) 所示的时间差分图像,图像上可以较为清楚地看到原来被忽视的沙尘气溶胶纹理,再将差分增强图像上沙尘气溶胶作为示踪物,得到如图 2(c) 所示的风矢量。

与 2011 年 4 月 30 日 6:00 的 NCEP 再分析资料的 850 hPa 风场(图 2(d)) 的相应区域进行对比,可以看出,反演得到的晴空风场呈西北风向,NCEP 再分析资料相应区域内风场也是西北风向;在内蒙中部平均风速为 8 m/s,相比 NCEP 再分析资料的相应区域略偏小 4—6 m/s;而在山西北部地区反演得到的平均风速与 NCEP 再分析资料的相应区域有较好的一致性。

5 结 论

利用大气辐射传输模式,结合 FY-2E 静止卫星红外通道光谱响应函数,提出使用基于红外窗区大气辐射传输方程的时间差分法从卫星云图提取微弱的晴空区气溶胶示踪信号的方法,并模拟计算了半小时内气溶胶消光系数 50% 的增量对卫星观测亮温增量的贡献。从模拟结果可以看出,春季大气条件下,半小时内气溶胶消光系数 50% 的增量能引起亮温变化 -0.379 K,且在 2 km 以下其贡献最大。气溶胶消光系数增量为 30% 时对应的红外窗区亮温的变化为 -0.210 K,也能够大于 FY-2E 红外窗通道灵敏度。这表明了在一定条件下,静止气象卫星红外窗通道云图上无云区反演边界层大气运动矢量的可能性。

基于时间差分法,进行实际个例分析,结果表明这种方法能够获得沙尘爆发区域内常规卫星导风技术所无法获得的风场信息,且与 NCEP 850 hPa 再分析资料有较好的一致性,对于监测预报沙尘移动及沙漠等风场观测资料极其缺乏的测站提供了风场信息的有益补充。

反演结果同时表明,由于基于时间差分法的晴空区沙尘气溶胶移动信号提取技术依赖于短时间内沙尘气溶胶移动的增量对于卫星红外通道亮温的影响,沙尘气溶胶在短时间内移动越明显,对于卫星红外通道亮温增量的影响越大,图像中可追踪的特征点越多,本方法的可适用性就越好,导风精度就应该越高;如果短时间内沙尘气溶胶没有明显的移动,则难以提取沙尘移动信息,进而难以作为晴空区导风的示踪物。另外,本文仅利用理论模拟计算及较少个例对该方法进行验证,有待于进一步对该方法的大气条件、地域和季节等适应性进行系统地研究探讨。沙尘气溶胶导出风矢的高度,主要是在边界层内,但更加细化的高度指定方法也有待于进一步研究。

参考文献(References)

Berk A, Anderson G P, Acharya P K, Hoke M L, Chetwynd J H, Bernstein L S, Shettle E P, Matthew M W and Adler-Golden S M. 2003. MODTRAN 4 Version 3 Revision 1 User's Manual, Manual, Air Force Research Laboratory. Hanscom Air Force Base, MA: Air Force Res Lab

Elterman L. 1970. Vertical-Attenuation model with Eight surface Meteorological Ranges 2 to 13 Kilometers. Environment Research Paper, NO. 318, AFCRL-70-200

关佳欣, 李成才. 2010. 我国中、东部主要地区气溶胶光学厚度的分布和变化. 北京大学学报(自然科学版), 46(2): 186-191

何立明, 王华, 阎广建, 李小文, 朱文娇, 王锦地. 2003. 气溶胶光学厚度与水平气象视距相互转换的经验公式及其应用. 遥感学报, 7(5): 372-378

罗云峰, 李维亮, 周秀骥. 2001. 20 世纪 80 年代中国地区大气气溶胶光学厚度的平均状况分析. 气象学报, 59(1): 77-87

Nann S and Riordan C. 1991. Solar spectral irradiance under clear and cloudy skies: measurements and a semiempirical model. Journal of Applied Meteorology, 30(4): 447-462 [DOI: 10.1175/1520-0450(1991)030<0447:SSIUCA>2.0.CO;2]

石广玉. 2007. 大气辐射学. 北京: 科学出版社, 261-264

沈建国, 李嘉鹏, 牛生杰, 姜学恭. 2007. 沙尘天气中气溶胶光学特性的时空分布特征. 中国沙漠, 27(3): 495-501

Schmetz J, Holmlund K, Hoffman J, Strauss B, Mason B, Gaertner V, Koch A and Van De Berg L. 1993. Operational cloud-motion winds from Meteosat infrared images. Journal of Applied Meteorology, 32(7): 1206-1225 [DOI: 10.1175/1520-0450(1993)032<1206:OCMWFM>2.0.CO;2]

Stewart T R, Smith W L and Hayden C M. 1985. A note on water-vapor wind tracking using VAS data on McIDAs. Bulletin of the American Meteorological Society, 66(9): 1111-1115 [DOI: 10.1175/1520-0477(1985)066<1111:ANOWVW>2.0.CO;2]

苏志侠, 吕世华, 罗四维. 1999. 美国 NCEP/NCAR 全球再分析资料及其初步分析. 高原气象, 18(2): 209-218

Velden C S, Hayden C M, Nieman S J, Menzel W P, Wanzong S and Goerss J S. 1997. Upper-Tropospheric Winds Derived from Geostationary Satellite Water Vapor Observations. Bulletin of the American Meteorological Society, 78(2): 173-195 [DOI: 10.1175/1520-0477(1997)078<0173:UTWDFG>2.0.CO;2]

王毅. 2004. 大气内目标背景对比度及大气能见度的研究. 合肥: 中国科学院安徽光学精密机械研究所

王振会, 曾维麟. 1996. 卫星云迹风微机客观导出系统. 南京气象学院学报, 19(1): 69-75

詹奕哲, 王振会, 张治国. 2012. FY-2E 分裂窗晴空沙尘区导风初步研究. 遥感学报, 16(4): 738-750

Zhang J H, Mao J T and Wang M H. 2002. Analysis of the aerosol extinction characteristics in different areas of China. Advances in Atmospheric Sciences, 19(1): 136-152 [DOI: 10.1007/s00376-002-0040-x]

朱彦良, 凌超, 陈洪滨, 张金强, 彭亮, 余予. 2012. 两种再分析资料与 RS92 探空资料的比较分析. 气候与环境研究, 17(3): 381-391